Influence of solid–liquid interactions on dynamic wetting: a molecular dynamics study

Influence of solid–liquid interactions on dynamic wetting: a molecular dynamics study

Emilie Bertrand, Terence D Blake[1] **and Joël De Coninck**

Centre de Recherche en Modélisation Moléculaire (CRMM), Avenue Copernic 1, Parc Initialis, 7000 Mons, Belgium

E-mail: emilie.bertrand@crmm.umh.ac.be, terrydblake@btinternet.com and joel.de.coninck@crmm.umh.ac.be

Abstract

Large-scale molecular dynamics (MD) simulations of liquid drops spreading on a solid substrate have been carried out for a very wide range of solid–liquid interactions and equilibrium contact angles. The results for these systems are shown to be consistent with the molecular-kinetic theory (MKT) of dynamic wetting, which emphasizes the role of contact-line friction as the principal channel of energy dissipation. Several predictions have been confirmed. These include a quantitative link between the dynamics of wetting and the work of adhesion and the existence of an optimum equilibrium contact angle that maximizes the speed of wetting. A feature of the new work is that key parameters (κ^0 and λ), normally accessible only by fitting the MKT to dynamic contact angle data, are also obtained directly from the simulations, with good agreement between the two sources. This validates the MKT at some fundamental level. Further verification is provided by contact angle relaxation studies, which also lend support to the interfacial tension relaxation process invoked in Shikhmurzaev's hydrodynamic model of dynamic wetting.

1. Introduction

When a liquid drop is placed in contact with a solid substrate, it spreads spontaneously towards its equilibrium shape, with a dynamic contact angle θ_D starting from $180°$ and relaxing to its static value θ_S. Because of contact angle hysteresis, θ_S may be greater than θ^0, the equilibrium contact angle given by Young's equation. During spreading, the velocity of the contact line V_{CL} falls from some initially high value towards zero. For a given system under a given set of conditions, $\theta_D = f(V_{CL})$. The principal driving force for spreading is provided by the change in surface free energy; for small drops, gravity can usually be neglected. Since the shape of the drop changes, energy is dissipated. Aside from viscous losses within the bulk of the drop, there are two principal channels for dissipation due to the presence of the moving contact line at which the liquid–vapour interface meets the solid surface [1–5][2]:

- viscous flow in the narrow wedge of liquid near the contact line;
- dissipation associated with the expansion of the solid–liquid interface in the immediate vicinity of the contact line.

Both channels may contribute to the observed changes in θ_D.

The first channel is characterized by the shear viscosity of the liquid η_L and can be described by hydrodynamics. For viscous liquids at small dynamic angles, this can be the dominant mode, especially for receding contact lines and completely wetting liquids. Models of dynamic wetting

---

[2] In the case of complete wetting ($\theta^0 = 0$), the surface pressure of the liquid on the solid may cause a precursor film to form ahead of the drop. Flow within this film then provides an additional dissipation channel [3, 6]. Processes occurring at the leading edge of this film are presumably similar to those at an advancing contact line but are not considered explicitly here.

---

[1] Author to whom any correspondence should be addressed.
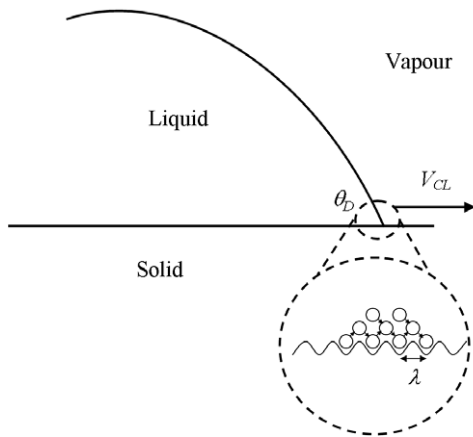
Figure 1. Representation of the moving contact line according to the molecular-kinetic theory.

that emphasize this channel, such as that of Voinov [1], Cox [7] and Dussan [8], have proved successful in accounting for the experimentally observed variation of θ_D in such cases (e.g. [3, 9–12]). Several schemes have been devised to accommodate the moving contact line within this flow. These have their limitations and are still a matter of some debate [11, 13].

The second channel is characterized by molecular interactions near the contact line. An innovative way of incorporating these effects within the hydrodynamic framework has been proposed by Shikhmurzaev [13, 14]. However, despite considerable success in explaining a wide range of dynamic wetting behaviour in a consistent way, this approach awaits universal acceptance and would benefit from independent verification of its key parameters. An earlier model of dissipation within this small region, that neglects the hydrodynamics, the so-called molecular-kinetic theory (MKT) [15, 16], has also been successful in accounting for much of the observed behaviour of the dynamic contact angle in both experiment and simulation (e.g. [10–12, 16, 17]). In this model, the key parameters are κ^0, the equilibrium frequency of random molecular displacements occurring at the contact line, and λ, the average distance of each displacement. These are usually accessed by fitting dynamic contact angle data, but would again benefit from some means of independent assessment. It is this model that will be explored in the present paper within the context of large-scale molecular dynamics (MD) simulations.

As computer power has grown, MD simulations have proved to be an increasingly effective tool for exploring dynamic wetting phenomena (e.g. [11, 17–28]). Significantly, detailed comparisons between the simulations and the predictions of the MKT have tended to validate the latter at some fundamental level. For example, the molecular parameters (κ^0 and λ) obtained by fitting the MKT to dynamic contact angle data from simulations of spreading drops have been shown to agree rather well with the same parameters obtained by analysing the statistics of the molecular behaviour observed within the simulations [17, 25, 28].

Quite recently, the MKT has been extended to show how κ^0 might be estimated, *a priori*, from equilibrium

wetting properties, specifically the reversible work of adhesion between the liquid and the solid written in terms of the equilibrium contact angle: $Wa_{SL}^0 = \gamma_L(1 + \cos\theta^0)$ [29]. Supporting evidence was drawn from both experiment and some early simulations. Additional data have since been obtained by Vega *et al* [30]. Moreover, in just the last year, Ray *et al* [31] have published an extensive experimental study of dynamic wetting on carefully engineered surfaces of widely varying wettability that provides perhaps the strongest evidence to date of the predicted relationship between the dynamics of wetting and Wa_{SL}^0.

In what follows, we present new results of large-scale simulations of spreading drops carried out for a very wide range of solid–liquid interactions and corresponding values of θ^0 and Wa_{SL}^0. The data are analysed at the molecular level and compared with the predictions of the MKT applied to the global behaviour of the drop. The work is an extension of an earlier study carried out in this laboratory by de Ruijter *et al* [17, 32]. As we will show, our findings do indeed support the idea that equilibrium wetting properties have a strong and broadly predictable effect on wetting dynamics. We commence with an outline of the MKT. Details of the MD model and the droplet spreading simulations are given in sections 3 and 4. Results are presented in section 5 and compared with the MKT. Section 6 deals with independent verification of κ^0 and λ. Our conclusions are summarized in section 7.

2. Molecular-kinetic theory

The first description of dynamic wetting to take account of the dissipation at the contact line due to interactions with the solid was given by Blake and Haynes [15, 16, 33]. According to their view, the movement of the contact line is determined by the statistical dynamics of the molecules within the three-phase zone (TPZ) where the solid, liquid and gas phases meet. At the molecular scale, this zone has a finite size, comparable with the thickness of its component interfaces, but is otherwise unspecified (figure 1).

As noted above, the key parameters are κ^0, the equilibrium frequency of random molecular displacements or 'jumps', occurring within the TPZ, and λ, the average distance of each jump. The frequency κ^0 is related to the depth of the potential wells within the energy landscape of the solid surface, while λ is related to their separation. When the contact line is stationary, the frequency of jumps in the forward and backward directions is the same: $\kappa^+ = \kappa^- = \kappa^0$, and there is no net flux. Dissipation occurs when this equilibrium is displaced by an applied force leading to the net displacement of the contact line. Dynamic wetting is then seen as a classical stress-modified rate process. The variation in the dynamic contact angle is due to the disturbance of local adsorption equilibria, and hence to changes in the local surface tensions as the contact line moves across the solid surface. These changes in the surface tensions give rise to the driving force required to restore equilibrium $F_w = \gamma_L(\cos\theta^0 - \cos\theta_D)$, which is then dissipated through the molecular interactions and eventually appears as heat.

Application of Frenkel–Eyring theory [34, 35] to this process gives the following simple equation for the contact-line velocity:

$$V_{CL} = 2\kappa^0 \lambda \sinh\left(\frac{\gamma_L(\cos\theta^0 - \cos\theta_D)}{2nk_BT}\right), \qquad (1)$$

where n is the number of adsorption sites per unit area of the solid surface, k_B is the Boltzmann constant and T the temperature. The equilibrium frequency κ^0 is related to the specific activation free energy of wetting per unit area Δg_w^* by

$$\kappa^0 = \frac{k_BT}{h} \exp\left(\frac{-\Delta g_w^*}{nk_BT}\right), \qquad (2)$$

where h is the Planck constant.

If the adsorption sites are distributed uniformly and molecules move only between adjacent sites, then $n \approx 1/\lambda^2$. In this case, (1) contains only two unknown parameters, κ^0 and λ, the values of which can be obtained by fitting the equation to experimental data. While the fitted value of λ is usually found to be of molecular dimensions, κ^0 can vary widely [11, 16, 36] and generally decreases with increasing liquid viscosity.

The effect of viscosity on κ^0 is accounted for by supposing that Δg_w^* is the sum of contributions from both viscous interactions between the liquid molecules Δg_{LL}^* and interactions between the liquid molecules and the solid Δg_{SL}^*, $\Delta g_w^* = \Delta g_{LL}^* + \Delta g_{SL}^*$. The Eyring theory of viscous flow [34] gives $\Delta g_{LL}^* = nk_BT \ln(\eta_L v_L/h)$, where v_L is the volume of the unit of flow. Substitution in (2) then gives

$$\kappa^0 = \frac{k_BT}{\eta_L v_L} \exp\left(\frac{-\Delta g_{SL}^*}{nk_BT}\right). \qquad (3)$$

Thus, κ^0 is inversely dependent on η_L, as observed.

The next step is to estimate Δg_{SL}^*. Since this depends on the solid–liquid interactions, it seems reasonable to suppose that it must be related to the reversible work of adhesion Wa_{SL}^0. This is equivalent to assuming that the depth of each potential-energy well is related to Wa_{SL}^0/n. If so, then to a first approximation we can write $\Delta g_{SL}^* = \gamma_L(1 + \cos\theta^0)$ [29], whence

$$\kappa^0 = \frac{k_BT}{\eta_L v_L} \exp\left(\frac{-\gamma_L(1 + \cos\theta^0)}{nk_BT}\right). \qquad (4)$$

Substitution in (1) then gives a formula with just one unknown, the molecular jump length λ. Equation (4) is one of the key relationships we have investigated in the present work.

If the system is not too far from equilibrium, i.e. θ_D is not too different from θ^0, then the argument of the sinh function in (1) will be small and the expression reduces to the linear form

$$V_{CL} = \frac{\kappa^0 \lambda}{nk_BT} \gamma_L(\cos\theta^0 - \cos\theta_D), \qquad (5)$$

which may be written more simply as

$$V_{CL} = \frac{1}{\zeta_{CL}^0} \gamma_L(\cos\theta^0 - \cos\theta_D), \qquad (6)$$

where $\zeta_{CL}^0 = \frac{nk_BT}{\kappa^0\lambda} \approx \frac{k_BT}{\kappa^0\lambda^3}$ is termed the coefficient of contact-line friction between the liquid and the solid [17].

This coefficient determines the rate of dissipation in the linear regime and has the same units as viscosity. Furthermore, we can link it to θ^0 via (4):

$$\zeta_{CL}^0 \approx \frac{\eta_L v_L}{\lambda^3} \exp\left(\frac{\gamma_L(1 + \cos\theta^0)}{nk_BT}\right). \qquad (7)$$

Contact-line dissipation should therefore increase linearly with viscosity but exponentially with solid–liquid interaction. Evidence supporting the latter prediction has been found from experiment and MD simulation [29–31].

One consequence of this result is that, because both the driving force for wetting F_W and the contact-line friction increase with solid–liquid interactions, there may be an optimum wettability that maximizes the rate of wetting. Specifically, it is predicted that there will be an optimum θ^0 that maximizes the contact-line speed as θ_D approaches 180°, and this θ^0 will be greater than zero whenever

$$\frac{2\gamma_L}{nk_BT \ln 3} > 1. \qquad (8)$$

The maximum will occur at

$$\theta_{Opt}^0 = \cos^{-1}\left(\frac{nk_BT \ln 3}{\gamma_L} - 1\right). \qquad (9)$$

Qualitative evidence for this behaviour can be found in the patent literature [37].

3. Simulation model

Here we describe the main elements of the simulations: the potentials, the specific parameters and the simulation characteristics. The general approach and parameter values follow previous simulations where we studied spreading on flat [17, 32] and porous surfaces [38], fibre wetting [25, 39, 40], capillary imbibition [23, 41, 42] and dewetting [27].

3.1. Liquid

The liquid molecules are eight-atom chains, denoted L. By considering chains rather than single atoms, we increase the viscosity of the liquid to more realistic values and considerably reduce evaporation into the surrounding vacuum, which facilitates the analysis. This strategy is consistent with previous simulations of wetting dynamics [20, 21, 27, 32, 43, 44].

To maintain a constant distance between any two adjacent atoms within a given molecule, we incorporate a confining potential between nearest neighbours i and j

$$U_{conf}(r_{ij}) = Ar_{ij}^6, \qquad (10)$$

where r_{ij} is their distance of separation. The power 6 is chosen for computational convenience [32]. The constant A is derived from the Lennard-Jones interaction parameters (see section 3.3) and is defined as $A = \varepsilon_{LL}/(\sigma_{LL})^6$, where ε_{ij} and σ_{ij} are related to the depth of the potential well and the effective atomic diameter, respectively. U_{conf} and ε_{LL} are expressed in the same units of energy, and r_{ij} and σ_{LL} in the same units of distance.

Table 1. Liquid and solid properties of the simulation model for $T = 33.33$ K and $r_c = 2.5\sigma$.

Property			
Liquid density	ρ_L	1.826 ± 0.007	10^{-2} atom Å^{-3}
Solid density	ρ_S	1.712	10^{-2} atom Å^{-3}
Surface tension	γ_L	2.49 ± 0.65	mN m^{-1}
Diffusion coefficient	$(D_{diff})_L$	56.3 ± 2.1	Å^3 ns^{-1}
Shear viscosity	η_L	0.248 ± 0.004	mPa s

3.2. Solid

The solid substrate is a square planar lattice with periodic boundary conditions, comprising three atomic layers. Each solid atom, denoted S, is placed at a lattice node 3.93 Å from its four nearest neighbours, corresponding to $2^{1/6}\sigma_{SS}$, i.e. the equilibrium distance between two atoms interacting through the Lennard-Jones potential. The atoms of the solid vibrate thermally around their initial equilibrium position according to a harmonic potential of the form

$$U_h(\vec{r}_i) = B|\vec{r}_i - \vec{r}_i^0|^2 \qquad (11)$$

with $\vec{r}_i$ the instantaneous position of a solid atom i and $\vec{r}_i^0$ its equilibrium position [27, 44]. The constant B is also derived from the Lennard-Jones parameters and is defined as $B = 2.5(\varepsilon_{SS}(\sigma_{SS})^2)$. While very simple, this specification provides a realistic solid surface that can exchange energy with the liquid, yet is sufficiently rigid and impermeable.

3.3. Interaction

For simplicity, we assume that the principal interactions within our system can be described by a pair-wise Lennard-Jones potential:

$$U_{LJ}(r_{ij}) = 4\varepsilon_{ab}\left[C_{ab}\left(\frac{\sigma_{ab}}{r_{ij}}\right)^{12} - D_{ab}\left(\frac{\sigma_{ab}}{r_{ij}}\right)^6\right]. \qquad (12)$$

For convenience, the same values of $\varepsilon_{ab} = 33.33$ K (4.6×10^{-22} J) and $\sigma_{ab} = 3.5$ Å are used for the different types of interaction: L–L, S–S and L–S. This assignment is arbitrary, but allows us to set the values systematically [23] and also ensures that the L–S interactions are consistent with the Lorentz–Berthelot rules. We use the usual cut-off radius of $r_c = 2.5\sigma$ to truncate the Lennard-Jones potential and keep the computations manageable. The constants C_{ab} and D_{ab} enable us to selectively increase or decrease the coupling between different types of atoms. We set $C_{LL} = D_{LL} = C_{SS} = D_{SS} = 1$, but keep C_{SL} and D_{SL} variable to allow us to modify the liquid–solid interactions and hence θ^0.

3.4. Simulation characteristics

To define a timescale for our simulations, it is necessary to assign masses to the atoms. For all the atoms (L and S) we used $m_L = m_S = 12$ g mol^{-1}, i.e. the molar mass of carbon. Once again, this choice is arbitrary but does not affect our results qualitatively and allows us to compare them with other related studies.

The time step between computational iterations is 0.005 ps and the neighbour list is updated every 10 iterations. In preparation for subsequent data analysis, the xyz positions of the atoms are recorded periodically at intervals of 100 to 10 000 time steps depending on the kind of analysis required.

All the simulations are carried out at a temperature of 33.33 K, which is kept constant during the equilibration period using a thermostat based on velocity scaling and applied to the liquid and solid separately. During a spreading simulation or the measurement of liquid properties, velocity scaling is applied only to the solid substrate. This allows us to mimic an isothermal solid realistically without introducing non-physical behaviour into the liquid.

3.5. Liquid and solid properties

These are required in order to analyse our results and are listed in table 1.

The surface tension of our liquid was measured from the pressure tensor for a free liquid film with planar L–V interfaces according to the method described previously [27].

The shear viscosity η_L was determined from the diffusion coefficient $(D_{diff})_L$ via the Stokes–Einstein relation:

$$(D_{diff})_L = \frac{k_B T}{6\pi\eta_L r_p}, \qquad (13)$$

where r_p is the radius of a probe particle. The diffusion coefficient was obtained by measuring the mean square displacement of atoms over long times. For a 3D trajectory we have [45, 46]

$$(D_{diff})_L = \frac{1}{(2\times 3)}\frac{1}{N}\lim_{t\to\infty}\frac{d}{dt}\left\langle\sum_{i=1}^{N}|\vec{r}_i(t) - \vec{r}_i(t_0)|^2\right\rangle, \qquad (14)$$

where $\vec{r}_i(t_0)$ is the position of atom i at starting time t_0 and $\vec{r}_i(t)$ its position at time t. The brackets $\langle\,\rangle$ stand for the average over several starting times.

We first equilibrated a spherical drop of 216 320 atoms, of radius $\sim$140 Å. The drop was generated from an initial cube over a period of 3×10^5 iterations, which is long enough to achieve equilibrium, and we ran the measurements over an additional 10^6 time steps. The xyz positions of all the atoms were recorded every 10^3 time steps. The resulting file allowed us to follow the displacements of those atoms that remained within an inner sphere of 70 Å. This volume is of sufficient size to give a reliable result, but small enough to ensure we measure only bulk properties free of any influence of the surface. We took six different starting times and averaged our results. This gave $(D_{diff})_L = 56.25 \pm 2.05$ Å^2 ns^{-1}, which yields $\eta_L = 0.248 \pm 0.004$ mPa s. The same diffusion coefficient was obtained if we followed the displacement of the centre of mass of a molecule instead of the motion of individual atoms. This is logical, since the atoms of a given molecule cannot diffuse independently over an extended distance.

4. Droplet spreading simulations

Having defined our system in terms of its potentials and parameters and determined the general properties of our liquid,

we can proceed to study the spreading process by examining the behaviour of a liquid drop when it is brought into contact with the solid. Specifically, we study the evolution with time of the contact angle $\theta_D(t)$ and base radius $R(t)$ for a wide range of solid–liquid interactions and, therefore, a wide range of θ^0.

4.1. System construction

To build our system in a consistent way, we construct a spherical drop of typically 5000 molecules (40 000 atoms) of radius 77.7 Å above the centre of a planar circular solid substrate comprising 66 102 atoms. The radius of the solid is four times larger than that of the drop. This allows sufficient space for the liquid to spread without reaching the edge of the solid. The drops are formed by first equilibrating a larger cube of 27 040 molecules (216 320 atoms) for 3×10^5 time steps and then extracting the required drop from the centre of the cube.

Next, we allow the drop and the solid to equilibrate independently for 10^5 iterations at constant temperature, with the drop placed in the vacuum above the substrate at a distance of 100 Å. The drop is then moved into contact with the solid and spreading starts. From this moment, only the temperature of the solid is controlled. The position of each atom of the liquid is measured every 10^3 iterations, allowing us to extract the contact angle of the drop and its base radius from each snapshot. Drops are followed for 2×10^6–8×10^6 iterations (10–40 ns), until spreading stops or the contact angle ceases to change within the noise of the simulation.

To determine the contact angle and base radius at any instant, we must first locate the liquid–vapour interface. Details of the method have been given in previous publications [17, 27, 32]. In brief, we divide the drop into horizontal layers 3 Å in thickness (small enough to give sufficient layers while retaining a uniform density within each layer). By symmetry, we determine the centre of these layers and calculate the density of atoms as a function of the radial distance from the centre. The radius of each layer is then given as the distance from the centre at which the density falls below a selected cut-off value, typically 85% of the central density. We checked that our results did not depend on our choice of this cut-off value. Once we have the profile of the drop, we can study its evolution with time in a way that mimics real experiments.

To measure the contact angle, we find the best circular fit to the measured profile. The first two layers in contact with the solid are omitted from the fit, since this part of the drop deviates from its otherwise spherical form [47]. The circular fit is then extrapolated to the position of the first liquid atoms. The tangent to the circle at this position gives the contact angle and the base radius. We have checked that this location gives a constant drop volume. Figure 2 illustrates the technique.

In our simulations, 18 levels of liquid–solid interaction were investigated by varying the coupling coefficients in the Lennard-Jones potential $C_{SL} = D_{SL}$ from 0.2 to 1.3 in steps of 0.05 or 0.1. Figure 3 gives a typical profile view of the system at equilibrium for four different liquid–solid interactions. For the lowest couplings (0.2–0.5), equilibrium was achieved rapidly, which made the data rather noisy and
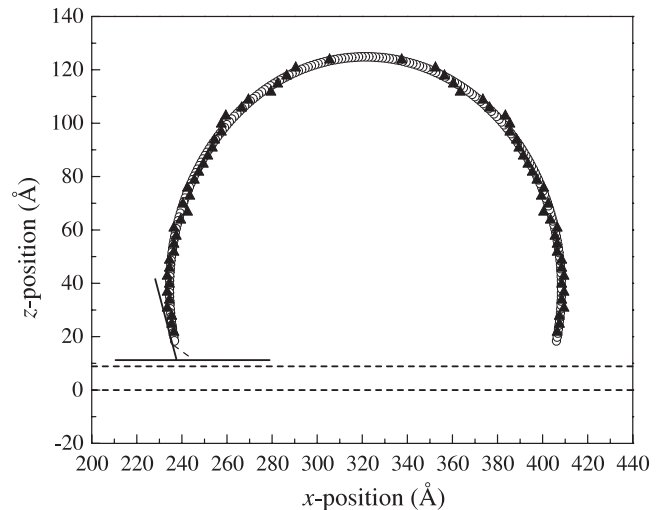
Figure 2. Profile of the drop at equilibrium on the solid substrate, with $C_{SL} = D_{SL} = 0.6$. Upper and lower surfaces of the solid substrate are represented by the horizontal dashed lines. The first two layers of liquid in contact with the solid are omitted. Filled triangles delineate the edge of the drop, and open circles show the fitted circular profile.

analysis of the dynamics difficult. We therefore repeated these simulations with a much bigger drop containing 27 040 molecules (216 320 atoms) having a radius of 140 Å. The number of atoms in the solid was correspondingly increased to 104 535. This yielded more stable data to characterize the dynamics and allowed us to verify that our results were not dependent on the size of the simulation.

5. Spreading dynamics

Here we compare our MD results with the theoretical predictions of the MKT. Results for drops of 216 320 atoms with couplings $C_{SL} = D_{SL}$ from 0.2 to 0.5 are shown in figure 4(a); results for the smaller drop of 40 000 atoms with couplings $C_{SL} = D_{SL}$ from 0.55 to 1.1 are shown in figure 4(b). In each case, the dynamic contact angle starts from 180° and relaxes to its equilibrium value after a period that increases with the coupling. Thereafter, no change in angle is detectable within the noise of the simulation. Couplings 1.1, 1.2 and 1.3 all gave complete wetting, with the contact angle tending asymptotically to zero at long times (>40 ns). Couplings 0.2–1.1 are therefore sufficient to cover the whole range of wettability investigated. The corresponding values of θ^0 (0°–166°) are summarized in table 2 (below). Except in the case of complete wetting, they are given as the average values over the plateau region together with their standard deviations.

5.1. Fitting procedures

In previous work, contact angle relaxation data $\theta_D(t)$ from simulation and experiment were compared directly with the MKT [17, 32, 49]. It was assumed that the drop remained spherical throughout spreading, thus providing a link between
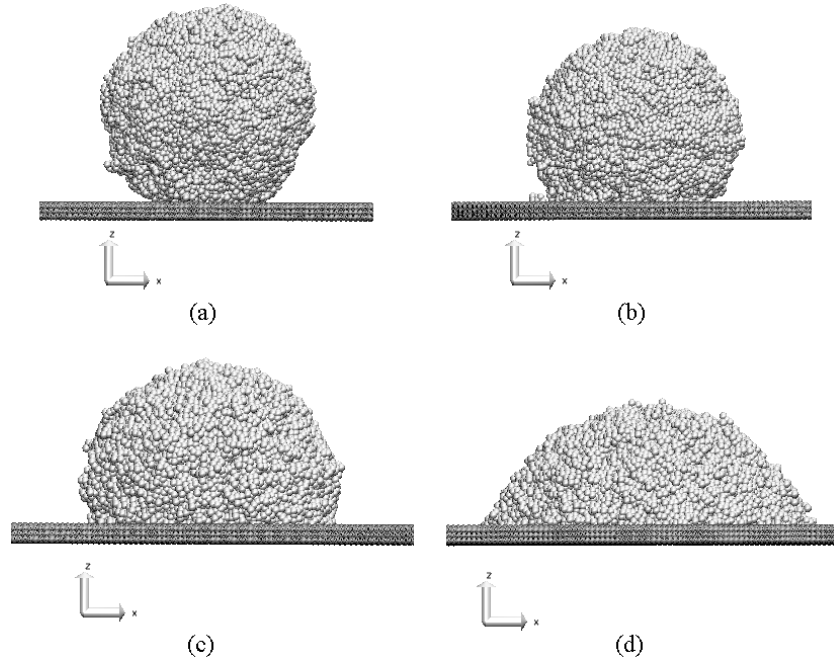
Figure 3. Typical profiles of a 40 000 atom drop at equilibrium on the solid substrate with four different couplings and, thus, different equilibrium contact angles and base radii: $C_{SL} = D_{SL} =$ (a) 0.2, (b) 0.4, (c) 0.6 and (d) 0.8. The 3D images were generated using VMD software [48].
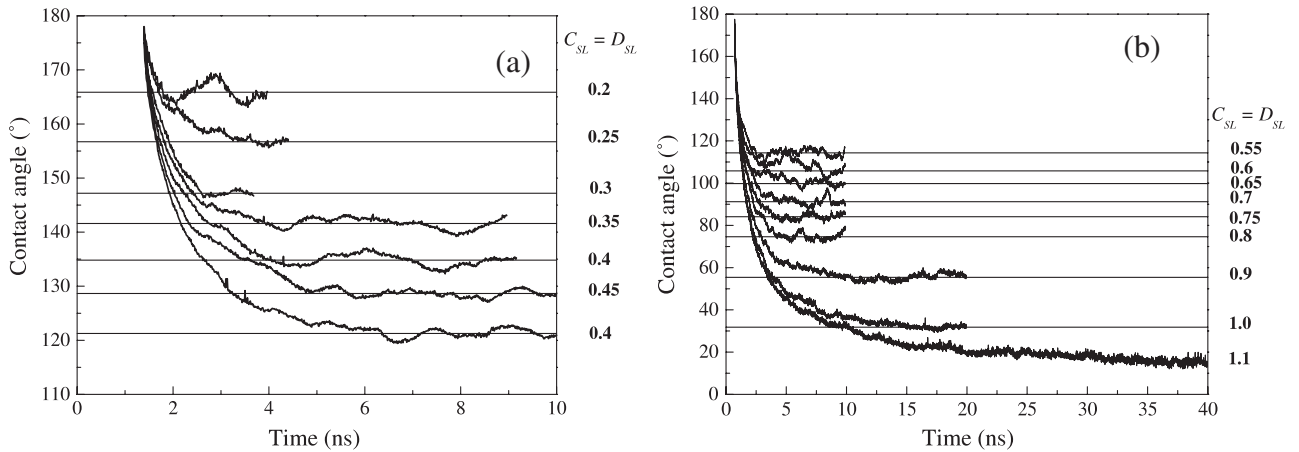
Figure 4. MD data for spreading drops of 216 320 atoms (a) or 40 000 atoms (b) for couplings $C_{SL} = D_{SL} = 0.2$–1.1. The horizontal lines indicate the equilibrium contact angles θ^0.

the base radius R and the droplet volume V. Since the liquid was of low volatility, V was constant; hence,

$$\frac{dR}{dt} = V_{CL} = -\frac{d\theta_D}{dt} \left(\frac{3V}{\pi} \right)^{1/3} \frac{(1 - \cos\theta_D)^2}{(2 - 3\cos\theta_D + \cos^3\theta_D)^{4/3}}. \quad (15)$$

Combining (15) with (1) then gave a linked pair of differential equations. Provided γ_L was known, these could be solved using a fourth-order Runge–Kutta algorithm to give $\theta_D(t)$, which could then be fitted to the data with κ^0 and λ treated as adjustable parameters. In cases where the dynamic contact angle data did not deviate far from equilibrium, equation (6) replaced (1), yielding just the contact-line friction coefficient ζ_{CL}^0. The frequency κ^0 could then be determined only if λ could be estimated, or vice versa.

The above procedure, though effective, has the disadvantage of being rather time consuming and sensitive to the initial values of the parameters used in the fit. An alternative and statistically more robust approach has therefore been adopted here [50]. Recognizing that equations (1) and (6) give V_{CL} as a function of θ_D, the $R(t)$ data are first fitted by a ratio of polynomials

$$R_{fit}(t) = \frac{\sum_{k=0}^{k_{max}} a_k t^k}{1 + \sum_{k=1}^{k_{max}} b_k t^k}, \quad (16)$$

using a Levenberg–Marquardt algorithm together with the bootstrap method [51] to give an analytical expression, from which $V_{CL}(t)$ and its estimated error can be obtained by simple differentiation. Here, a_k and b_k are the free parameters to be adjusted and $k_{max} = 10$. The function satisfies the limits

**Table 2.** Equilibrium contact angle θ^0, jump frequency κ^0 and contact-line friction coefficient ζ_{CL}^0 obtained from the droplet spreading data. The value of λ was set at 4.3 ± 0.4 Å.

Coupling $C_{LS} = D_{LS}$	θ^0 (deg.)	ζ_{CL}^0 (mPa s)	κ^0 (10^{10} Hz)
0.2	165.9 ± 1.6		
0.25	156.7 ± 0.5		
0.3	147.2 ± 0.4		
0.35	141.6 ± 1.0	0.089 ± 0.024	6.55 ± 3.63
0.4	134.8 ± 1.1	0.157 ± 0.043	3.70 ± 2.04
0.45	128.0 ± 0.7	0.222 ± 0.060	2.62 ± 1.44
0.5	121.3 ± 0.8	0.212 ± 0.056	2.74 ± 1.49
0.55	114.3 ± 1.6	0.252 ± 0.069	2.30 ± 1.27
0.6	105.8 ± 2.4	0.364 ± 0.096	1.60 ± 0.87
0.65	99.8 ± 1.4	0.466 ± 0.126	1.25 ± 0.69
0.7	91.2 ± 1.9	0.429 ± 0.114	1.35 ± 0.73
0.75	84.1 ± 1.3	0.425 ± 0.113	1.37 ± 0.74
0.8	74.6 ± 1.7	0.528 ± 0.140	1.10 ± 0.60
0.9	55.4 ± 1.6	0.749 ± 0.197	0.777 ± 0.422
1.0	31.8 ± 0.8	0.868 ± 0.227	0.667 ± 0.361
1.1	0	1.100 ± 0.291	0.528 ± 0.287

Figure 5. Typical density profile in the first liquid layer near the solid substrate for a drop of 40 000 atoms and coupling $C_{SL} = D_{SL} = 0.6$ (open circles). The sigmoidal function used to describe the profile is shown by the line.

$R_{\text{fit}}(t = 0) = a_0$ and $R_{\text{fit}}(t \to \infty) = a_l/b_l$, where l is the order of the best polynomial, i.e. that which minimizes the error but still gives $R_{\text{fit}}(t)$ as a concave increasing function. The radius dynamics can therefore be fitted without additional assumptions. Since we also measure $\theta_D(t)$, then for each time t we now have the measured dynamic angle and the calculated contact-line velocity together with their associated errors. The complete set of $V_{CL}(t)$ and $\theta_D(t)$ data are then fitted to (1) or (6) using the Levenberg–Marquardt algorithm to give κ^0, λ and ζ_{CL}^0. If one has only $\theta_D(t)$ data, the same approach can be taken by using the spherical cap approximation to generate the initial $R(t)$ data set.

Before fitting the MD data, certain precautions are necessary. At the start of the dynamics, we have large contact angles and relatively large contact-line velocities. These points are therefore heavily weighted in the fit. Our data for $\theta_D(t)$ and $R(t)$ are based on the assumption that the drop has a spherical profile at all times. However, this may not be valid immediately after contact between the drop and the solid, when inertial effects may modify the shape dictated by capillarity. Indeed, inspection of the earliest profiles reveals that the drop does not become spherical until some time after contact. As an initial filter, we could simply discard all the data taken before we have visual agreement between the radius given by the fitted circular profile and that measured directly. For the smaller drops this corresponds to the first 0.5–0.7 ns, depending on the couplings. For the larger drops the period is 1.3–1.6 ns. However, this procedure is rather subjective. We have therefore introduced a supplementary criterion based on direct measurement of R.

To do this, we examine the radial density profile in the first liquid layer in contact with the solid. We select shells 1 Å thick, centred on the axis of the drop, and compute the atomic density as a function of the distance from the axis. This is illustrated in figure 5. The profile can be fitted by a sigmoidal function [52], allowing us to locate the contact line and, hence, the base radius at each time during spreading. The resulting
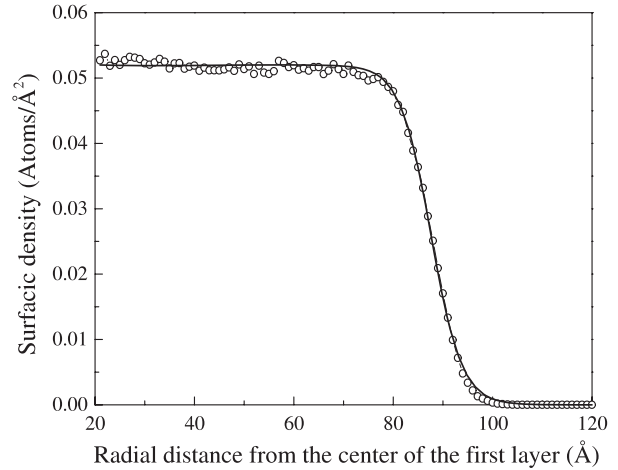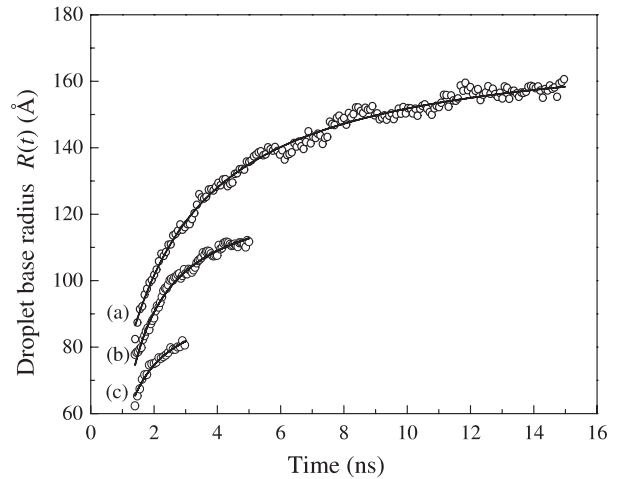

Figure 6. Growth of the base radius of a 40 000 atom liquid drop during spreading at couplings $C_{SL} = D_{SL}$ of (a) 1.0, (b) 0.8 and (c) 0.6 (open circles). The lines indicate the fits to (16).

$R(t)$ is then compared with that obtained by fitting the circular profile. We then consider the MD data to be useable once there is agreement between both techniques. This test is more objective and allows us to confirm our initial visual assessment. Because the circular fits ignore the first two layers, these tend to give slightly smaller values of R than we get by analysing the first layer directly. We therefore apply a small correction based on the difference at equilibrium.

Once we have selected the useable data, we can commence the fitting procedure. Since the MKT is meant to be universal, it should not matter which part of the dynamics we study. We therefore fit the $R(t)$ data to (16) for eight different starting times. Figure 6 gives examples of the behaviour of the base radius for a liquid drop of 40 000 atoms at couplings $C_{SL} = D_{SL} = 1.0, 0.8$ and 0.6. Also shown are the relevant fits to (16), which yield $V_{CL}(t)$ on differentiation.
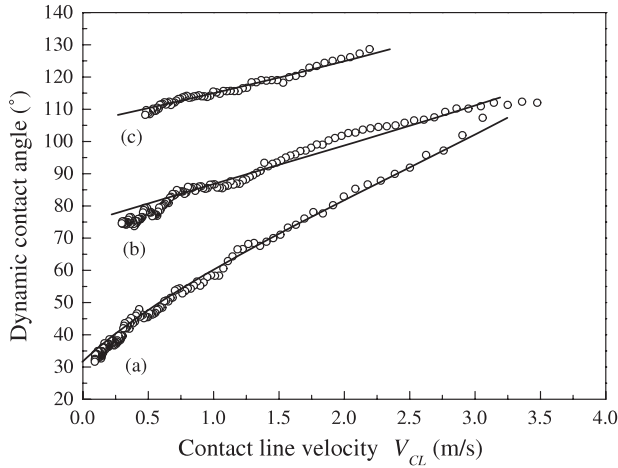
Figure 7. Typical behaviour of $\theta_D(V_{CL})$ during the spreading of a 40 000 atom drop at couplings $C_{SL} = D_{SL}$ of (a) 1.0, (b) 0.8 and (c) 0.6. The fits to (6) are shown by the smooth curves.
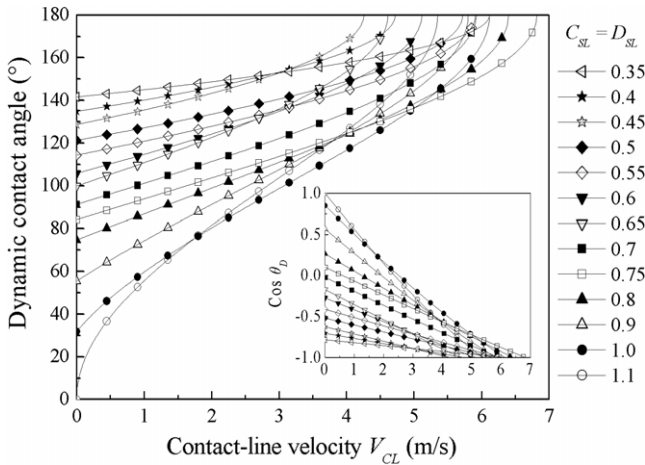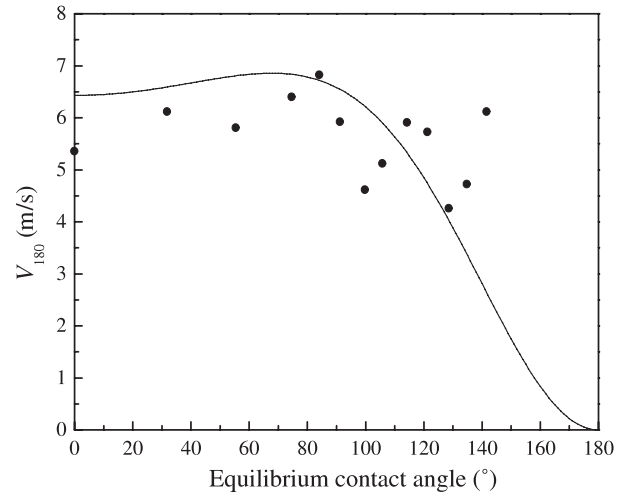

Figure 8. Velocity dependence of the contact angle for $C_{SL} = D_{SL} = 0.35$–1.1, plotted using the inverse of equation (1) with values of θ^0, κ^0 and λ from table 2. Symbols are used to distinguish the different curves.

5.2. Comparison with the MKT

Since γ_L is small (2.49×10^{-3} N m^{-1}) and we discard the highest velocities, the argument of the sinh function in (1) will tend to be small over the range of our data. As we show below (section 6.3), the jump distance λ in the simulations is 4.3 ± 0.4 Å, independent of the coupling. This gives $\gamma_L \lambda^3 / 2k_B T \sim 0.5$ and indicates that our data are in the linear regime described by equation (6) and characterized by ζ_{CL}^0. While it is possible to fit the data with even greater precision using (1), the resulting values of κ^0 and λ are correlated through ζ_{CL}^0 and are not robust. We therefore fit the $\theta_D(t)$ and the eight sets of $V_{CL}(t)$ data to (6) for each liquid–solid coupling using the known values of γ_L and θ^0. The multiple fits enable us to check that our procedure is consistent and to estimate the errors on κ^0 and ζ_{CL}^0.

Typical results are given in figure 7. At the lowest couplings (0.2–0.3), spreading was too rapid and the statistical


Figure 9. Dependence of the maximum velocity of wetting V_{180} on the equilibrium contact angle. The curve shows the theoretical dependence assuming $\Delta g_{SL}^* \sim W a_{SL}^0$. The filled circles are the individual values from figure 8.

noise too great to yield stable fits even for the larger drops. For the remaining couplings (0.35–1.1), the results in terms of the contact-line friction coefficient ζ_{CL}^0 and the jump frequency κ^0 are listed in table 2, together with their standard deviations. The values of κ^0 were calculated using the constant value $\lambda = 4.3 \pm 0.4$ Å. We also confirmed that the general MKT equation (1) gives the same values of κ^0 when fitted with the imposed value of λ.

Before proceeding, it is helpful to examine the overall way in which the dynamics of wetting in our simulations depends on the level of solid–liquid interactions, i.e. on θ^0. In figure 8, the dynamic contact angle θ_D is plotted as a function of V_{CL} for each coupling, using the inverse of equation (1) with the values of θ^0, κ^0 and λ from table 2. The original MD data are omitted for clarity. Two features are worthy of comment. First, the curves are rather linear, especially when plotted as $\cos \theta_D(V_C)$ (see the inset), thus validating our choice of (6) for the fits. Second, the curves show that as θ_D approaches 180° the highest wetting speeds are attained at couplings that give intermediate equilibrium contact angles. Except for the two lowest couplings, the curves initially extend to higher speeds as θ^0 is increased and then retreat. This is fully consistent with theory.

As we saw in section 2, if $\Delta g_{SL}^* \sim W a_{SL}^0$, the MKT predicts an optimum equilibrium contact angle that maximizes contact-line speed whenever condition (8) is satisfied [29]. Calculation shows that for the simulated system the LHS of this inequality is ~ 1.5, hence a weak maximum is expected. Based on equation (9), the highest wetting speed should occur for $\theta^0 \sim 70°$. Figure 9 shows a plot of V_{180}, the predicted contact-line velocity at which $\theta_D = 180°$, versus θ^0. This was calculated by combining equations (1) and (4), setting $\cos \theta_D = -1$. The site density n in (4) was assumed equal to the number of atoms per unit area of the solid surface, 6.47×10^{18} m^{-2}, since all the atoms contribute to the work of adhesion and their spacing determines the distribution of potential-energy wells (see figure 16, below). Comparing
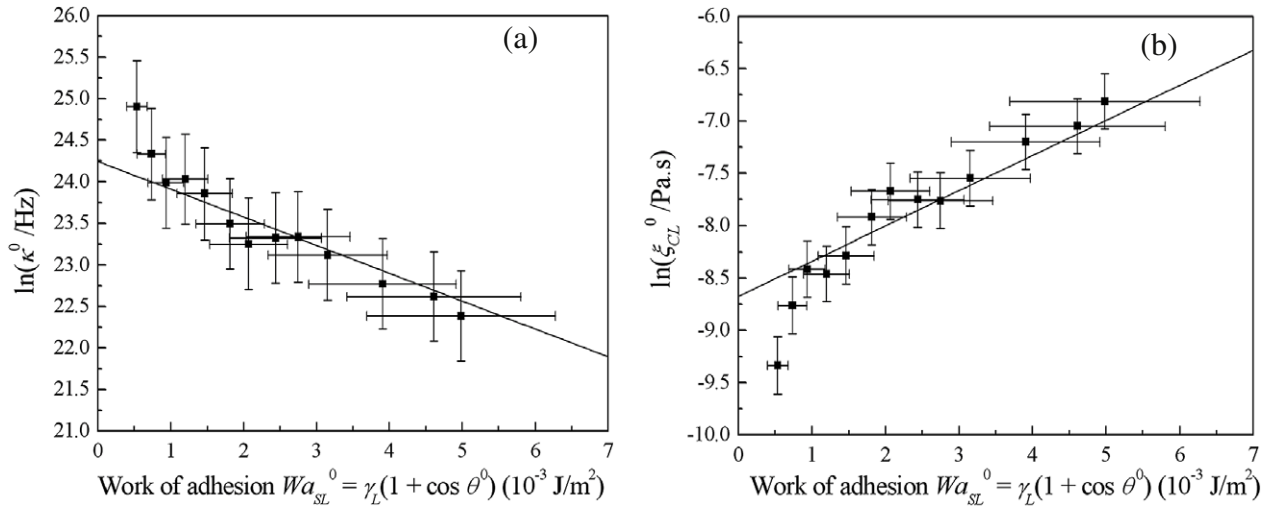
Figure 10. (a) $\ln \kappa^0$ and (b) $\ln \zeta_{CL}^0$ versus the work of adhesion Wa_{SL}^0 for spreading drops with $C_{SL} = D_{SL} = 0.35$–1.1. The lines show the relationships predicted by (4) and (7), respectively.

the theoretical curve with the individual values of V_{180} from figure 8 reveals broad agreement except at the lowest coupling, for which the uncertainty on κ^0 is comparatively large. This result not only implies that (4) is substantially correct, i.e. that $\Delta g_{SL}^* \sim Wa_{SL}^0$ for our system, it gives a direct indication of the significant and complex way in which equilibrium wetting properties can affect dynamic wetting.

Turning now to the specific influence of solid–liquid interactions on κ^0 and ζ_{CL}^0, equations (4) and (7) predict that $\ln \kappa^0$ should decrease linearly with Wa_{SL}^0 or $\cos \theta^0$, while $\ln \zeta_{CL}^0$ should increase. Figure 10 confirms that these predictions are well born out by our results, except at the lowest coupling. Indeed, the agreement with theory is remarkable. The lines through the data are not fits. They are those given by (4) and (7) using the system parameters from table 1 plus $\nu_L = 5.48 \times 10^{-31}$ m^3, and $n = 6.47 \times 10^{18}$ m^{-2}, without adjustment. The flow volume ν_L was estimated as the volume of one segment of a liquid molecule (i.e. one-eighth of the molecular volume). This seems reasonable, as the molecules are very flexible (polymer-like) and can move only into holes that appear within the liquid. These holes tend to be of segment size. The site density n was assumed equal to the number of atoms per unit area of the solid surface, as above.

6. Verification of fitting parameters κ^0 and λ

As we have seen, the MKT accounts for the dynamics of spreading in our simulations very well. However, the fact that a theory can fit some data is not sufficient to prove it valid. Some independent assessment of the fitting parameters is essential. One of the advantages of MD simulations is that they allow us to look very closely at the atomic motions, something that is impossible in a real experiment where the molecular scale is inaccessible. In what follows, we therefore study the random thermal displacements of the atoms at equilibrium to determine κ^0 and λ *directly* and compare them with the fitted values. Strategies for the direct measurement of κ^0 and λ have already
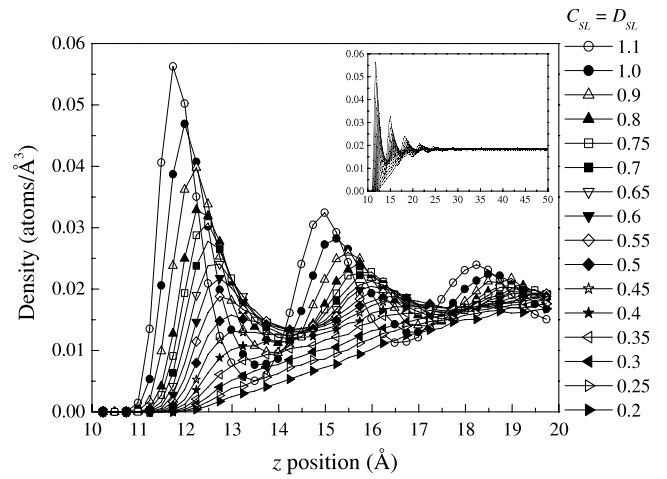

Figure 11. Mean density profiles of the liquid in the z-direction for $C_{SL} = D_{SL} = 0.2$–1.1. The surface of the solid (at $z = 8.86$ Å) is defined as the plane through the centres of the top layer of solid atoms.

been developed by De Coninck *et al* [17, 28, 32, 40, 53]. The approach taken here is similar, but with refinements to reduce ambiguity and improve precision.

The first step is to determine the equilibrium density profile in the z-direction normal to the solid surface. This is done by computing the atomic density within 0.25 Å thick horizontal slices starting at the solid and working outward into the bulk. The mean density profiles $\rho(z)$ obtained for each of the couplings between 0.2 and 1.1 are plotted in figure 11.

As previously observed in MD simulations [17, 40, 54–56], the liquid is strongly layered near the solid at high couplings. As the coupling is reduced, the layering becomes progressively less pronounced, until at $C_{SL} = D_{SL} = 0.2$ the profile resembles that of the liquid–vapour interface. Far away from the solid (>25 Å), any layering decays and the liquid has a uniform density equal to that of the bulk $\rho_L = 1.826 \pm 0.007 \times 10^{-2}$ atoms Å^{-3} (figure 11, inset).
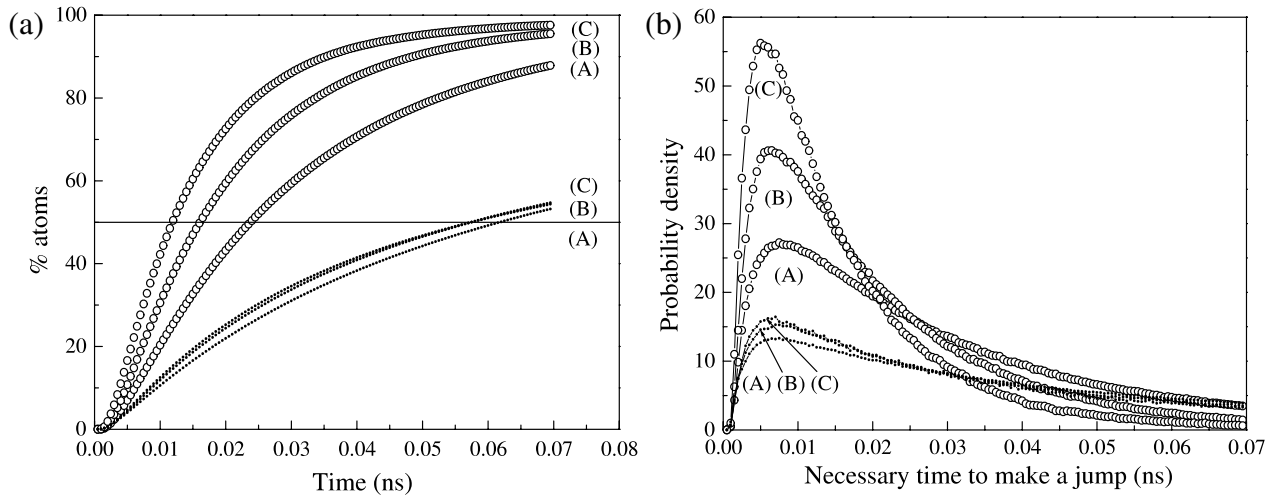
Figure 12. (a) Cumulative percentage of atoms from the first layer that have made a parallel (open circles) or perpendicular (small filled circles) jump as a function of time. The horizontal line indicates the time at which half the atoms have jumped. (b) Associated probability density distributions. The data are the average over 500 different starting times for a 40 000 atom drop with $C_{SL} = D_{SL}$ (A) 1.0, (B) 0.8 and (C) 0.6.

At equilibrium, liquid atoms adjacent to the solid surface undergo random thermal displacements, jumping from one potential well to the next and from one layer to another, but with no net flux, so that $\kappa^+ = \kappa^- = \kappa^0$. Displacements are in any direction (except into the solid), so there exist multiple definitions for jumps that contribute to contact-line motion. The equilibrium frequency κ^0 will be some average of all possible types of atom displacement. Nevertheless, due to the layering, these movements are likely to be anisotropic, with greater mobility within a given layer than between layers. We therefore divide the displacements into two categories:

- parallel jumps within the first layer at frequency $\kappa_\parallel^0$;
- perpendicular jumps between the first and second layers at frequency $\kappa_\perp^0$.

Ideally, we should focus on the molecular displacements within the TPZ, where the density profile $\rho(z)$ is inevitably modified by the proximity of the L–V interface. Since the TPZ is only a few atoms thick and subject to large fluctuations, this is not straightforward. However, motion of the contact line during spreading is possible only because of a net flux into the first layer. We therefore apply our analysis to the entire first layer, assuming uniform behaviour throughout.

From the density profile, we locate the first two layers at each coupling. A parallel jump is then defined as a jump within the first layer (in the xy-plane) of not less than $d_\parallel$, the distance between adjacent atoms in the solid surface, i.e. 3.93 Å. Smaller displacements are considered as thermal agitation. Because we are at equilibrium, the rate of jumping in a given direction will be the same as in the reverse. It is easier to count all jumps, both backwards and forwards, so we have to divide the result by 2 to determine $\kappa_\parallel^0$.

Similarly, a perpendicular jump is defined as a jump from the first layer to the second one, with a displacement along z of not less than $d_\perp$, the distance of separation between the two first peaks in the profile (slightly less than σ). Smaller jumps and rare jumps between layer 1 and layer 3 or beyond

are neglected. Since the rate of jumping from layer 1 to layer 2 will be the same as from layer 2 to layer 1, we need count the jumps in only one direction to determine $\kappa_\perp^0$.

The above definitions are essentially those used by de Ruijter *et al* [17, 32, 53] and could equally be applied here. However, to distinguish perpendicular and parallel jumps more precisely and so avoid the risk of double counting, we now introduce secondary criteria. A parallel jump is counted only if any associated displacement in the z-direction is less than $d_\perp$. Similarly, a perpendicular jump is counted only if any associated displacement in the xy-plane is less than $d_\parallel$. These restrictions have the advantage of separating perpendicular and parallel displacements into two distinct groups.

Once we have these definitions, we can analyse the xyz-file of all the atoms initially in the first layer (up to 5000) and follow them during the simulation to find the time necessary to make a jump. This analysis gives us distributions of jump distances and frequencies. To improve precision, we average over 500 different starting times $t > t_0$ (the time at which equilibrium is achieved). For the highest frequencies, the simulations are re-launched from equilibrium for a further 2×10^5 iterations with more frequent recording of the positions (every 100 time steps).

6.1. Jump frequency κ^0

Using the criteria described above, we can determine the cumulative percentage of atoms initially in the first layer that have made a parallel or perpendicular jump as a function of time. Typical results are given in figure 12(a) for a 40 000 atom drop at couplings $C_{SL} = D_{SL}$ (A) 1.0, (B) 0.8 and (C) 0.6. Several features are evident. There is a short induction time before the first atoms jump. The curves then tend to saturate at long times when all the atoms have had sufficient time to make a jump. Significantly, parallel displacements occur at a higher rate than perpendicular ones. Furthermore, the S–L coupling has a significant influence on both types of displacement: the

10
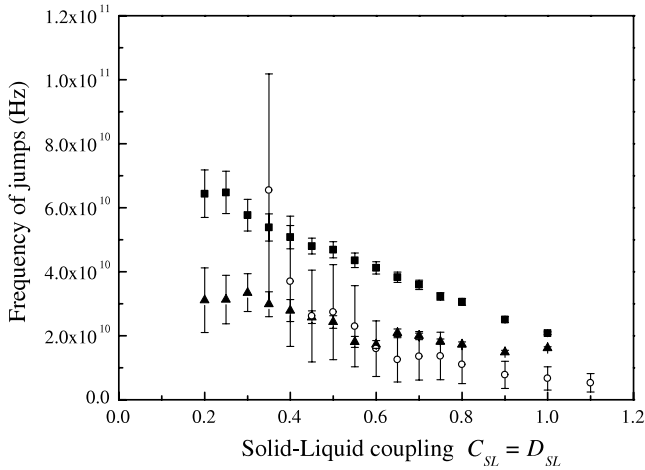
Figure 13. Frequency of jumps as a function of the coupling: $\kappa_{\parallel}^{0}$ (filled squares), $\kappa_{\perp}^{0}$ (filled triangles), κ^{0} from table 2 obtained by fitting the spreading dynamics with the MKT (open circles).

Figure 14. Time evolution of the peak density of the first layer near the solid surface, due to an instantaneous switch of the S–L coupling at $t = 0$, from $C_{SL} = D_{SL} = 0.2$–1.1. The curve is the best fit to (17).

bigger the coupling the lower the rate for both parallel and perpendicular jumps.

By differentiating the cumulative data, we obtain the probability density distributions of the time required to make a jump. These are given in figure 12(b). All have pronounced maxima but are skewed to long times. Ideally, we should consider the complete distribution to calculate the characteristic mean value of $\kappa_{\parallel}^{0}$ or $\kappa_{\perp}^{0}$ by inversion. To simplify the procedure, we assume that the average time for the collective movement of all the atoms is the time required for half the atoms of the first layer to have made a parallel or perpendicular jump [17, 28, 51]. This time is easily identified in figure 12(a). The characteristic frequency is then the inverse of this time, remembering to divide by 2 in the case of $\kappa_{\parallel}^{0}$. By repeating the counting procedure for each of the 500 starting times, we obtain average values of $\kappa_{\parallel}^{0}$ and $\kappa_{\perp}^{0}$ for each coupling together with their standard deviations. The results, together with the values of κ^{0} obtained by fitting the spreading dynamics with the MKT, are plotted in figure 13 as a function of the coupling.

Comparing the results, we see that $\kappa_{\parallel}^{0} > \kappa_{\perp}^{0}$, for all the couplings even though $d_{\perp} < d_{\parallel}$. This implies that the anisotropy of liquid displacement immediately adjacent to the solid is not simply due to the layering, since this is absent at the lowest couplings. It turns out that $\kappa_{\parallel}^{0} \sim 2\kappa_{\perp}^{0}$, so the difference may largely be due to the additional degree of freedom in the xy–plane. Furthermore, there is broad agreement between $\kappa_{\perp}^{0}$ and κ^{0} over a wide range of couplings, which confirms the result obtained by de Ruijter and co-workers for a more limited range [17, 32, 53]. Spreading is possible only if there is a net flux into the first layer. Because adsorption and desorption of atoms from the solid surface is less frequent than a displacement along the surface, the former becomes the rate-determining event for spreading in our system. The upward drift of κ^{0} at the lowest couplings is also logical. As the density of atoms in the first layer is reduced, adsorption–desorption events will play a decreasing role in dynamic wetting.
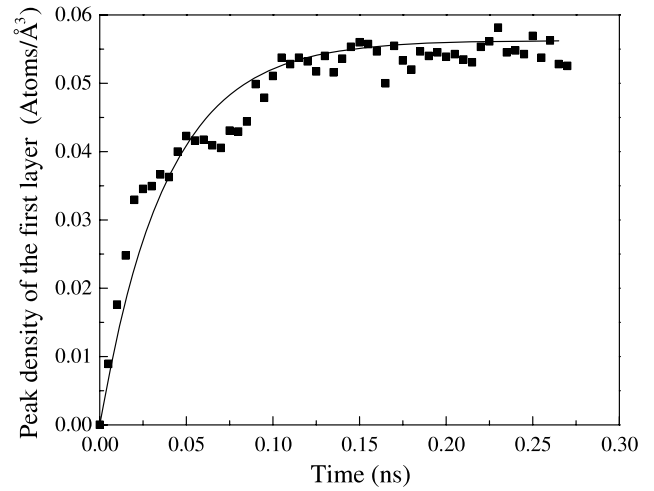
Inevitably, our definitions of parallel and perpendicular jumps are somewhat arbitrary. We have therefore checked what happens if we abandon the secondary criteria introduced here to avoid double counting and simply use the original definitions of de Ruijter. What we have found is that the values of $\kappa_{\parallel}^{0}$ are increased only slightly, whereas those of $\kappa_{\perp}^{0}$ are approximately doubled. This implies that successful parallel jumps are hardly contaminated by a perpendicular component, whereas about half of all perpendicular jumps have a significant parallel component. Again, this probably reflects the higher mobility within the bottom layer in comparison with that between the first two layers. However, whichever definition we use, the agreement between the measured rate of jumping and that found by applying the MKT to droplet spreading remains very good.

6.2. Interfacial relaxation

An alternative and completely independent approach to estimating κ^{0} is to determine the characteristic time for the S–L interface to relax from one state to another. Suppose we start with the system at equilibrium with $C_{SL} = D_{SL} = 0.2$ and then instantaneously switch the coupling from 0.2 to 1.1. Because the two couplings induce different density profiles (figure 11), the atoms at the interface will reorganize themselves. We can follow this reorganization by measuring the peak density in the first liquid layer ρ^{peak} as a function of time, and model it by a simple exponential:

$$\rho^{\text{peak}}(t) = \rho_{1.1}^{\text{peak}} + (\rho_{0.2}^{\text{peak}} - \rho_{1.1}^{\text{peak}}) \exp\left(-\frac{t}{\tau_{\text{relax}}}\right), \quad (17)$$

where $\rho_{1.1}^{\text{peak}}$ and $\rho_{0.2}^{\text{peak}}$ are the peak densities in the first layer for $C_{SL} = D_{SL} = 1.1$ and 0.2 respectively, and τ_{relax} is the characteristic relaxation time. An example is given in figure 14, where we see there is quite good agreement between the observed behaviour and (17). The fit gives $\tau_{\text{relax}} = 0.038 \pm 0.002$ ns,
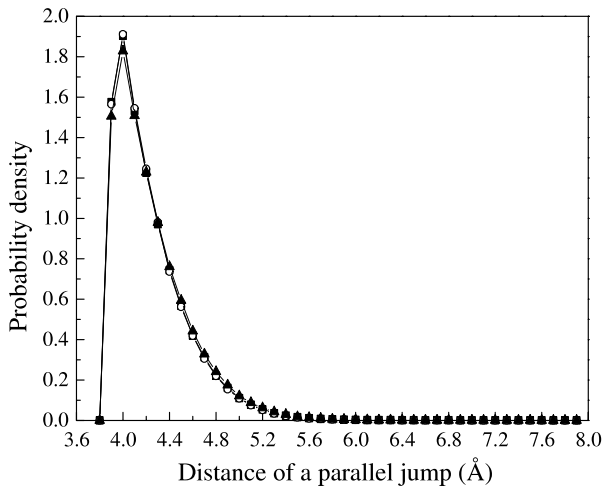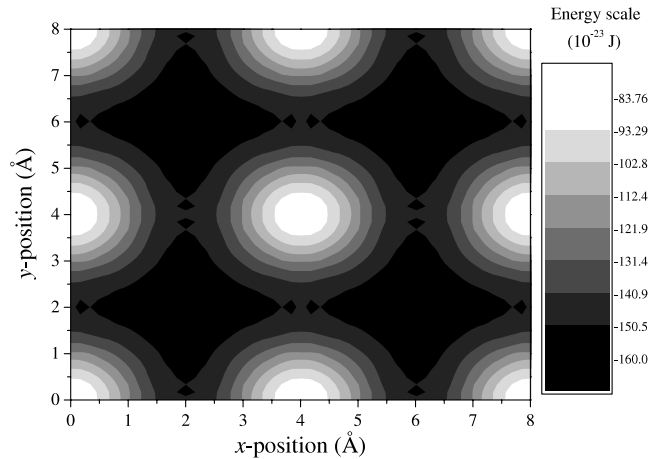
Figure 15. Distribution of the length of a jump in the first layer. The data represent the probability density for up to 5000 atoms in the first layer over 500 different starting times for a 40 000 atom drop at couplings $C_{SL} = D_{SL} = 1.0$ (filled squares), 0.8 (open circles) and 0.6 (filled triangles).

Figure 16. Contour map of the potential energy due to Lennard-Jones interactions for a single liquid atom interacting with the solid at distance σ from the surface, with $C_{SL} = D_{SL} = 1.0$. The white areas show the position of the solid atoms. The adsorption sites are located where the interactions are the most attractive (lowest energy), i.e. the dark areas between the solid atoms.

corresponding to a frequency $1/\tau_{relax} = 2.6 \pm 0.1 \times 10^{10}$ Hz. This is close to the value of κ^0 for a coupling of 0.55, i.e. about midway between the values for the initial and final states (figure 13). Thus, we can reasonably infer that the S–L interface relaxes at κ^0.

As well as giving greater confidence in the values of κ^0 found by applying the MKT, this conclusion also provides support for the interfacial tension relaxation process invoked in Shikhmurzaev's hydrodynamic model of dynamic wetting [13, 14, 57]. From the surface tension of the liquid and the change in the equilibrium contact angle, we can infer that the S–L interfacial tension changes by some 4.9 mN m^{-1} as the interface reorganizes. At a wetting speed of, say, 10 m s^{-1} (which is slightly larger than any in figure 8), a relaxation time of 0.038 ns implies that this gradient operates over a distance of less than 1 nm, i.e. within the dimensions of the TPZ. Nevertheless, as previously observed [58], the values of $1/\kappa^0$ found by applying the MKT to dynamic contact angle data for relatively viscous aqueous glycerol solutions on a polyester substrate are strikingly similar to the S–L interfacial relaxation times obtained by applying Shikhmurzaev's model to the same data. This agreement reflects a degree of commonality between the two models despite their radically different descriptive approach.

6.3. Jump distance λ

The jump distance can be investigated in much the same way as the frequencies. Results for the three couplings used for $\kappa_{\parallel}^0$ and $\kappa_{\perp}^0$ are given in figure 15. The probability distributions show that, unlike κ^0, λ does not depend on the coupling. This conclusion is consistent with the idea that the jump distance is related to the spacing of the potential wells (adsorption sites) at the solid surface and, therefore, to the lattice spacing. However, like the time distributions, those for the jump distance are asymmetric. They start at the minimum

value of 3.93 Å required to be counted as a jump, peak rapidly at about 4.0 Å, and then decay more slowly towards zero with a long tail. Consistent with our procedure for κ^0, we take the mean value given by the distribution as the characteristic value of λ for the collective motion of the contact line in our simulations, i.e. $\lambda = 4.3 \pm 0.4$ Å. This is the value we have used throughout this paper, notably in section 5.2 to fit our spreading data and determine κ^0 (table 2).

In previous studies, [17, 32, 40, 53], λ was taken simply as the distance between two atoms on the solid surface, i.e. $d_{\parallel}$. Evidently, the reality is more complex. The distribution of jump distances can be understood with reference to the potential-energy landscape experienced by a liquid atom at the surface of the solid. This is illustrated in figure 16. The geometry of the solid results in adsorption sites (places where the attraction is the greatest and the potential wells correspondingly deep) located between the solid atoms. A liquid atom can jump from any given site to any neighbouring one. However, simple quantization of the distance based on the lattice parameters will be prevented because each atom is tethered to its own molecular chain. A smooth distribution of jump distances therefore results. Since diagonal and longer jumps are possible, the mean value of λ is inevitably greater than $d_{\parallel}$.

7. Conclusion

The results presented here illustrate the value of large-scale molecular dynamics in modelling wetting and spreading at both global and molecular scales. Simulation is an important tool to help us understand the underlying physics. However, any conclusions must be tempered by an acknowledgment of the limitations imposed by current computational power and the relative simplicity of the systems we are able to investigate. Few of our simulations ran for more than 40 ns of notional real time; the largest drops studied were 140 Å in diameter, and intermolecular interactions (S–L and L–L) were governed

only by truncated Lennard-Jones potentials and Newton's laws. The liquid comprising our drops had a low density, surface tension and viscosity compared with a real liquid. The solid studied, though realistic in the sense that it was atomistic, rigid, impermeable and able to interact thermally with the liquid, was also atomically smooth and therefore free of the heterogeneities and roughness that characterize most of the solid surfaces encountered in the real world. Leaving aside the statistical fluctuations, wetting therefore proceeded smoothly, without any evidence of collective pinning events. Thus, one might conclude that both our system and our results are somewhat idealized. Nevertheless, systems such as those modelled here do provide a sound baseline for the behaviour we can expect to find in a real experiment. We can realistically expect that all the physics we see will be present in a real system. More complex surfaces will be investigated in the future. Some of the assumptions made in reaching our conclusions are no doubt open to challenge; however, we believe all the choices we have made are reasonable and defensible.

Our new work essentially refines and substantially extends that reported previously [17, 28, 32, 40]. We have confirmed that the dynamics of spreading and wetting in our system is described rather accurately by the molecular-kinetic theory, and that contact-line friction is the dominant channel of dissipation. By applying the MKT to our spreading data and also analysing the detailed behaviour on the atomic scale, we have been able not only to model the global behaviour of the dynamic contact angle as a function of contact-line speed, but to demonstrate that the key parameters in the model, κ^0 and λ, are an accurate reflection of the molecular motions at the atomic scale. Thus, the MKT appears valid at some fundamental level. Further verification has been provided by interfacial relaxation studies, which also lend support to Shikhmurzaev's hydrodynamic description of dynamic wetting and reflect a degree of commonality between the underlying models.

In addition, we have been able to confirm that the intrinsic wetting properties of the system as measured by the equilibrium contact angle θ^0 and work of adhesion Wa_{SL}^0 have a direct influence on the dynamics of wetting. Furthermore, this influence can be accounted for with good precision via equations (4) and (7) over a very wide range of equilibrium contact angles (up to at least 135°). The exponential nature of the dependence of κ^0 and ζ_{CL}^0 on Wa_{SL}^0 is clear evidence of the influence of the potential-energy landscape of the solid on wetting dynamics. The new results also demonstrate for the first time that, while κ^0 and ζ_{CL}^0 depend in a consistent way on the coupling between the liquid and the solid, λ is determined principally by the spacing of the adsorption sites on the solid surface and is therefore constant for our system. It is, however, slightly larger than the lattice spacing. One of the consequences of the link between κ^0 and Wa_{SL}^0 is that there exits an optimum θ^0 that maximizes the speed of wetting. This outcome has highly practical ramifications in diverse areas from high-speed coating to microfluidics.

References

[1] Voinov O V 1976 *Fluid Dyn.* **11** 714
[2] Petrov J G and Radoev B P 1981 *Colloid Polym. Sci.* **259** 753
[3] de Gennes P G 1985 *Rev. Mod. Phys.* **57** 827
[4] Brochard-Wyart F and de Gennes P G 1992 *Adv. Colloid Interface Sci.* **39** 1
[5] de Ruijter M J, De Coninck J and Oshanin G 1999 *Langmuir* **15** 2209
[6] Teletzke G F, Davis H T and Scriven L E 1987 *Chem. Eng. Commun.* **55** 41
[7] Cox R G 1986 *J. Fluid Mech.* **168** 169
[8] Dussan V E B, Rame E and Garoff S 1991 *J. Fluid Mech.* **230** 97
[9] Chen J D 1988 *J. Colloid Interface Sci.* **122** 60
[10] Petrov J G, Ralston J, Schneemilch M and Hayes R 2003 *J. Phys. Chem.* B **107** 1634
[11] Blake T D 2006 *J. Colloid Interface Sci.* **299** 1
[12] Ralston J, Popescu M and Sedev R 2008 *Annu. Rev. Mater. Res.* **38** 23
[13] Shikhmurzaev Y D 1997 *J. Fluid Mech.* **334** 211
[14] Shikhmurzaev Y D 1993 *J. Multiph. Flow* **19** 589
[15] Blake T D and Haynes J M 1969 *J. Colloid Interface Sci.* **30** 421
[16] Blake T D 1993 *Wettability* ed J C Berg (New York: Dekker) p 251
[17] de Ruijter M J, Blake T D and De Coninck J 1999 *Langmuir* **15** 7836
[18] Koplik J, Banavar J R and Willemsen J F 1989 *Phys. Fluids* A **1** 781
[19] Thompson P A and Robbins M O 1989 *Phys. Rev. Lett.* **63** 766
[20] Heine D R, Grest G S and Webb E B III 2003 *Phys. Rev.* E **68** 061603
[21] Heine D R, Grest G S and Webb E B III 2004 *Phys. Rev.* E **70** 011606
[22] Supple S and Quirke N 2004 *J. Chem. Phys.* **121** 8571
[23] Martic G, Gentner F, Seveno D, Coulon D, De Coninck J and Blake T D 2002 *Langmuir* **18** 7971
[24] Gentner F, Ogonowski G and De Coninck J 2003 *Langmuir* **19** 3996
[25] Seveno D, Ogonowski G and De Coninck J 2004 *Langmuir* **20** 8385
[26] Webb E B III, Grest G S, Heine D R and Hoyt J J 2005 *Acta Mater.* **53** 3163
[27] Bertrand E, Blake T D, Ledauphin V, Ogonowski G, De Coninck J, Fornasiero D and Ralston J 2007 *Langmuir* **23** 3774
[28] De Coninck J and Blake T D 2008 *Annu. Rev. Mater. Res.* **38** 1
[29] Blake T D and De Coninck J 2002 *Adv. Colloid Interface Sci.* **96** 21
[30] Vega M J, Gouttiére C, Seveno D, Blake T D, Voué M and De Coninck J 2007 *Langmuir* **23** 10628
[31] Ray S, Sedev R, Priest C and Ralston J 2008 *Langmuir* **24** 13007
[32] Blake T D, Clarke A, De Coninck J and de Ruijter M J 1997 *Langmuir* **13** 2164
[33] Blake T D 1968 The contact angle and two-phase flow *PhD Thesis* University of Bristol
[34] Glasstone S, Laidler K J and Eyring H J 1941 *The Theory of Rate Processes* (New York: McGraw-Hill)
[35] Frenkel J I 1946 *Kinetic Theory of Liquids* (Oxford: Oxford University Press)

[36] Wakeham W A, Assael M J, Marmur A, De Coninck J, Blake T D, Theron S A and Zussman E 2007 *Handbook of Experimental Fluid Mechanics* ed C Tropea, A L Yarin and J F Foss (Berlin: Springer) chapter 3, p 115

[37] Blake T D and Morley S D 1998 *US Patent Specification* 5792515

[38] Seveno D, Ledauphin V, Martic G, Voué M and De Coninck J 2002 *Langmuir* **18** 7496

[39] Seveno D and De Coninck J 2004 *Langmuir* **20** 737

[40] Seveno D, Ogonowski G and De Coninck J 2004 *Langmuir* **20** 8385

[41] Martic G, Gentner F, Seveno D, De Coninck J and Blake T D 2004 *J. Colloid Interface Sci.* **270** 171

[42] Martic G, Blake T D and De Coninck J 2005 *Langmuir* **21** 11201

[43] De Coninck J, D'Ortona U, Koplik J and Banavar J R 1996 *Phys. Rev.* E **53** 562

[44] Bertrand E, Blake T D and De Coninck J 2005 *Langmuir* **21** 6628

[45] Allen M P and Tildesley D J 1991 *Computer Simulation of Liquids* (New York: Oxford University Press)

[46] Rapaport D C 1995 *The Art of Molecular Dynamics Simulation* (Cambridge: Cambridge University Press)

[47] De Coninck J, Dunlop F and Menu F 1993 *Phys. Rev.* E **47** 1820

[48] Humphrey W, Dalke A and Schulten K 1996 *J. Mol. Graph.* **14** 33 http://www.ks.uiuc.edu/Research/vmd/

[49] de Ruijter M J, De Coninck J, Blake T D, Clarke A and Rankin A 1997 *Langmuir* **13** 7293

[50] Seveno D and De Coninck J 2009 submitted

[51] Press W H, Teukolsky S A, Vetterling W T and Flannery B P 1992 *Numerical Recipes in Fortran* 2nd edn (Cambridge: Cambridge University Press)

[52] Rawlinson J S and Widom B 1984 *Molecular Theory of Capillarity* (Oxford: Clarendon)

[53] de Ruijter M J 1998 A microscopic approach to partial wetting: statics and dynamics *PhD Thesis* University of Mons-Hainaut

[54] Saville G 1977 *Faraday* II **73** 1122

[55] Grigera J R, Kalko S G and Fischbarg J 1996 *Langmuir* **12** 154

[56] Priezjev N V, Darhuber A A and Troian S M 2005 *Phys. Rev.* E **71** 041608

[57] Shikhmurzaev Y D 2008 *Capillary Flows with Forming Interfaces* (Boca Raton, FL: Chapman and Hall/CRC)

[58] Blake T D and Shikhmurzaev Y D 2002 *J. Colloid Interface Sci.* **253** 196